Reactive control of large-scale structures in a turbulent wake

E. VARON[a], J.-L. AIDER[a,b], Y. EULALIE[c], S. EDWIGE[c], P. GILOTTE[c]

a. Laboratoire PMMH, CNRS UMR7636, ESPCI Paris, PSL Research University, 10 rue Vauquelin, Paris, France

b. Laboratoire PMMH, CNRS UMR7636, Université Pierre et Marie Curie, 10 rue Vauquelin, Paris, France

c. Plastic Omnium Auto Extérieur Services (POAES), Parc Industriel de la Plaine de l'Ain, Sainte-Julie, France

Abstract:

In this study we focus on the control of the dynamics of 3D turbulent wake downstream a square-back Ahmed body. The peculiar bimodal dynamics of such a geometry are first characterized through the trajectories of the pressure center over the rear part of the model and the recirculation barycenter in the wake. In particular it is shown that these dynamics allow the definition of three different states: the two so-called Reflectional Symmetry Breaking (RSB) modes and the transient symmetric mode. Then, using tangential continuous or pulsed blowing in three different regions along the upper edge of the rear part of the model the dynamics of the bimodal wake can be forced into a stable asymmetric state in open loop control. Finally, a simple closed-loop opposition control, based on real-time identification of the wake barycenter in PIV fields, forces the dynamics of the wake into a regular oscillatory motion at a well-defined frequency. Depending on the actuation parameters, the wake dynamics can also be switched from bimodal to multimodal behavior. Interestingly, the recirculation area (size of the recirculation bubble) is much more reduced for the closed-loop experiments when jets are pulsed rather than continuous. For the pulsed jets, the reduction is also increased when the proper frequency is chosen.

Keywords: Flow control, wake, turbulence.

1 Introduction

It is well-known that the turbulent wakes downstream 3D bluff-bodies can be very complex, exhibiting large-scale and small-scale coherent structures with strongly intermittent behaviors. Among the various 3D bluff-bodies, one of the most famous is the so-called "Ahmed body" which is a 3D model used in automotive aerodynamics to study the wake of a very simplified passenger car [1]. Depending on the geometry of the rear part, the overall structure of the wake changes together with the aerodynamic drag coefficient. One can find a competition between large scale streamwise longitudinal vortices [2], spanwise Kelvin-Helmholtz vortices, recirculation bubbles or toroïdal vortices. If the time-averaged velocity fields are relatively simple and well-defined, the instantaneous velocity fields are very complex and exhibits together large and small-scale structures leading to one of the most complex 3D turbulent

flows. It has been shown recently that square-back Ahmed body exhibits a peculiar behavior with a so-called bi-stable (or bimodal) wake [8]. Depending on the geometric parameters (aspect ratio of the bluff-body's cross-section, underbody flow), one can observe a right-left oscillation of the global wake. It was shown recently [11] that the large-scale slow-time dynamics behave like a chaotic system with two well-defined strange attractors. In this study we are interested in the control of the dynamics of the bimodal oscillation of the wake, not in the time-averaged drag coefficient nor in pressure coefficients.
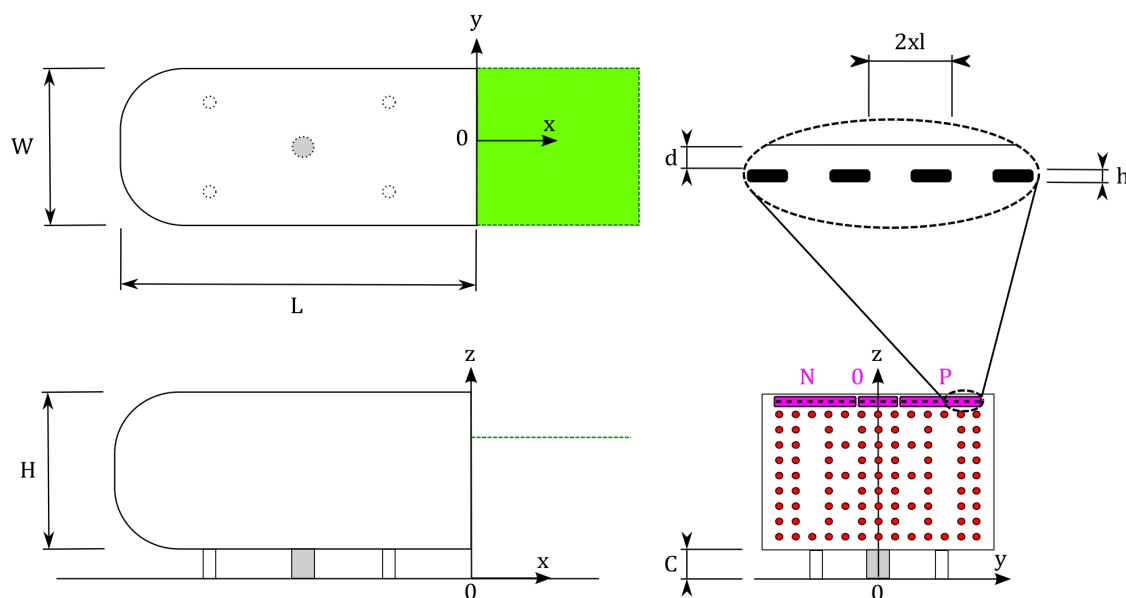
2   Experimental setup

Figure 1: Upper view (top left figure), side view (lower left figure) and view from behind (right figure) of the Ahmed body. The main PIV measurement plane is shown on top (green rectangle) and lower left (green line) figures. The rear part of the model is mapped with 95 pressure sensors (red circles on lower right figure). The actuator outputs are gathered in their jets group (pink): "N", "0" and "P". The bluff-body is fixed on the aerodynamic balance through a supplementary pod (grey part on lower figures).

2.1   Ahmed Body

The bluff body is a 0.7 scale of the original Ahmed body ($L = 0.731$ m long, $H = 0.202$ m high and $W = 0.272$ m wide), as described in [4]. The rear part of the model is a square-back geometry with sharp edges.

2.2   Wind-tunnel

Experiments are carried out in the PRISME laboratory wind-tunnel (Orléans, France). The model is mounted on a raised floor with a properly profiled leading edge and an adjustable trailing edge to avoid undesired flow separations. The ground clearance is set to $C = 5$ cm. In the following, the free-stream velocity is $U_\infty = 30$ m.s^{-1}, which corresponds to a Reynolds number based on the height of the model $Re_H = U_\infty H / \nu_{air} = 3.9 \times 10^5$ where ν_{air} is the kinematic viscosity of the air at ambient temperature. The origin is located on the rear of model ($x = 0$), in the vertical symmetry plane ($y = 0$) and on the

raised floor ($z = 0$). Nondimensionalization is applied to distances such as $x^* = x/H$, $y^* = y/H$, $z^* = z/H$ and the convective time is defined as $t^* = tU_\infty/H$.

2.3 Sensors

2.3.1 Pressure

The wall-pressure over the rear part of the model is studied using a set of 95 pressure vinyls defining an area denoted S_p and covering 70% of the entire surface S_r, as shown on Fig. 1. Each vinyl is 2 cm away from each of its neighbors. The sampling frequency for the pressure acquisition f_P depends on the acquisition time T_P: $f_P = 3 \times 10^4/T_P$. As we are interested in controlling the large-scale dynamics of the wake, a global indicator of the state of the wake can be inferred from the offline instantaneous pressure fields. We thus define the instantaneous wall pressure barycenter which can be seen as the footprint of the wake. Denoting the space average of a quantity a over an area S as $\langle a \rangle_S$, we compute the pressure barycenter at $x^* = 0$ as:

$$\overrightarrow{OG_p(t)} = \begin{pmatrix} y_p^*(t) \\ z_p^*(t) \end{pmatrix} = \begin{pmatrix} \frac{\langle y^* p(t) \rangle_{S_p}}{\langle p(t) \rangle_{S_p}} \\ \frac{\langle z^* p(t) \rangle_{S_p}}{\langle p(t) \rangle_{S_p}} \end{pmatrix}, \tag{1}$$

where $p(t) = p(y^*, z^*, t)$ is the local pressure measured at time t. Thus the instantaneous barycenter of the depression can be tracked at each time step as illustrated by the Fig. 2(a).
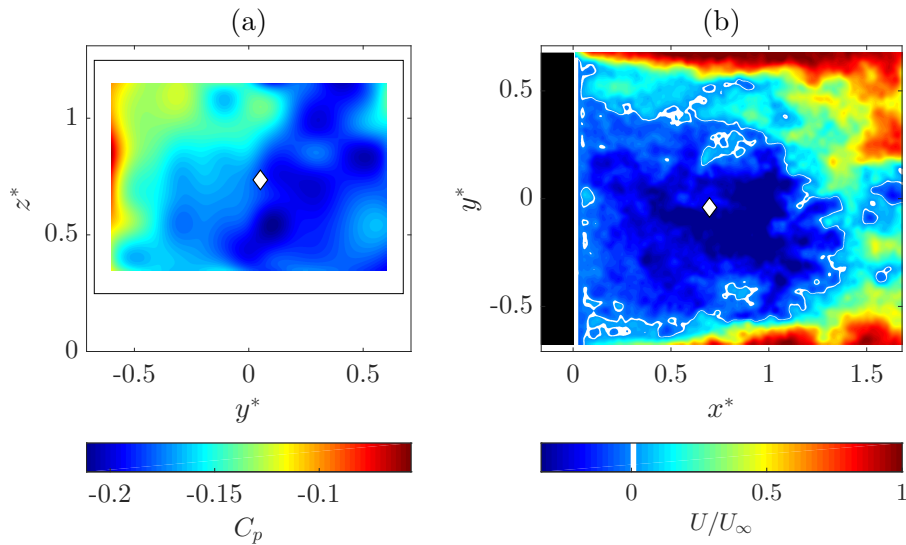

Figure 2: Typical (a) instantaneous pressure field over the rear part of the model and (b) instantaneous 2D velocity field in the horizontal plane shown in Fig. 1. The diamond (white) is the instantaneous barycenter position of respectively (a) the rear pressure G_p and (b) the intensity recirculation G_{rec}, which are introduced and discussed in the following section.

2.3.2 Velocity

The velocity fields are obtained using a standard particle image velocimetry (PIV) setup composed of the double-frame TSI camera PowerView Plus 4MP, streaming pair of snapshots on a computer and a

double-cavity pulsed YaG laser. The camera and the laser are synchronized, reaching a $7-$Hz sampling frequency. The investigated PIV planes are the horizontal planes at $z^* = 1.00$ and $z^* = 1.25$.

The two-dimensional two-components (2D-2C) velocity fields are computed in *real-time* at the frequency $f_{PIV} = 7$ Hz, using an optical flow algorithm implemented on the Nvidia GPU card GeForce GTX580. Unfortunately this frequency drops at 4 Hz for the recorded data due to the writing process. The interrogation window size is 16×16 pixels and the calculation is based on three iterations for each of the three pyramid reduction levels. One can find more details on this measurement method in [3, 9, 10] which rigorously demonstrate its offline accuracy. Gautier and Aider achieved the implementation of the algorithm on a GPU to enable high-frequency real-time computations of PIV fields in hydrodynamic experiments of closed-loop flow control [5, 7, 6]. An example of a 2D-2C instantaneous velocity field is shown in Fig. 2(b), where the complexity of the turbulent wake, with large and small-scale strongly fluctuating vortices can be seen. Quantities derived from these fields, such as the instantaneous recirculation area A_{rec}, the swirling strength λ_{Ci} or the Q-criterion, can then be computed in *real-time*.

In the same manner as for the pressure barycenter we define the instantaneous recirculation intensity barycenter from the velocity fields in the PIV horizontal plane at $z^* = 1$ as:

$$\overrightarrow{OG_{rec}(t)} = \begin{pmatrix} x^*_{rec}(t) \\ y^*_{rec}(t) \end{pmatrix} = \begin{pmatrix} \frac{\langle x^* u_{rec}(t) \rangle_{A_{rec}(t)}}{\langle u_{rec}(t) \rangle_{A_{rec}(t)}} \\ \frac{\langle y^* u_{rec}(t) \rangle_{A_{rec}(t)}}{\langle u_{rec}(t) \rangle_{A_{rec}(t)}} \end{pmatrix}, \tag{2}$$

where $u_{rec}(t) = u_{rec}(x^*, y^*, t)$ and $A_{rec}(t)$ are respectively the local streamwise component of the recirculation velocity and the recirculation area at time t. G_{rec} can be computed in *real-time* from the PIV fields and then be used as an input for a control law.

2.3.3   Aerodynamic forces

The bluff body is linked to a six-components aerodynamic balance through a cylindrical leg of diameter 32 mm localized at the center of the bottom face. This leg does not modify the reflectional symmetry of the square-back body and its influence is discussed in [11].

2.4   Actuators

The wake of the bluff-body is forced using five continuous or pulsed jets located $d = 10$ mm under the upper edge of the rear part of the model ($z^* = 1.25$). The jets are pulsed using three solenoid valves (Matrix) incorporated inside the model just upstream the blowing jets. Each jet is $l = 5.5$ mm away from each of its neighbors and its rectangular exhaust section is $l \times h = 5.5 \times 0.5$ mm^2. The jets angle relative to the horizontal plane is set to 0°. The normalized actuation frequency is defined as $f^*_{act} =$ are 0.2 and 0.8. The jet velocity u_{jet} can reach up to 100 m.s^{-1}. The momentum coefficient is $c_\mu = 0.03\%$.

Each solenoid is independently controlled and connected to a jets group: "N", "0" and "P". As described by Fig. 1, "N" contains the eight jets located in the negative part of the y-axis, whereas "P" contains the eight jets located in the positive part. Finally "0" contains the four central jets.

3   Reference flow

The unforced flow is described in Ref. [11], highlighting that the dynamics of large-scale structures can be tracked either by the pressure center either by the recirculation barycenter since both are highly
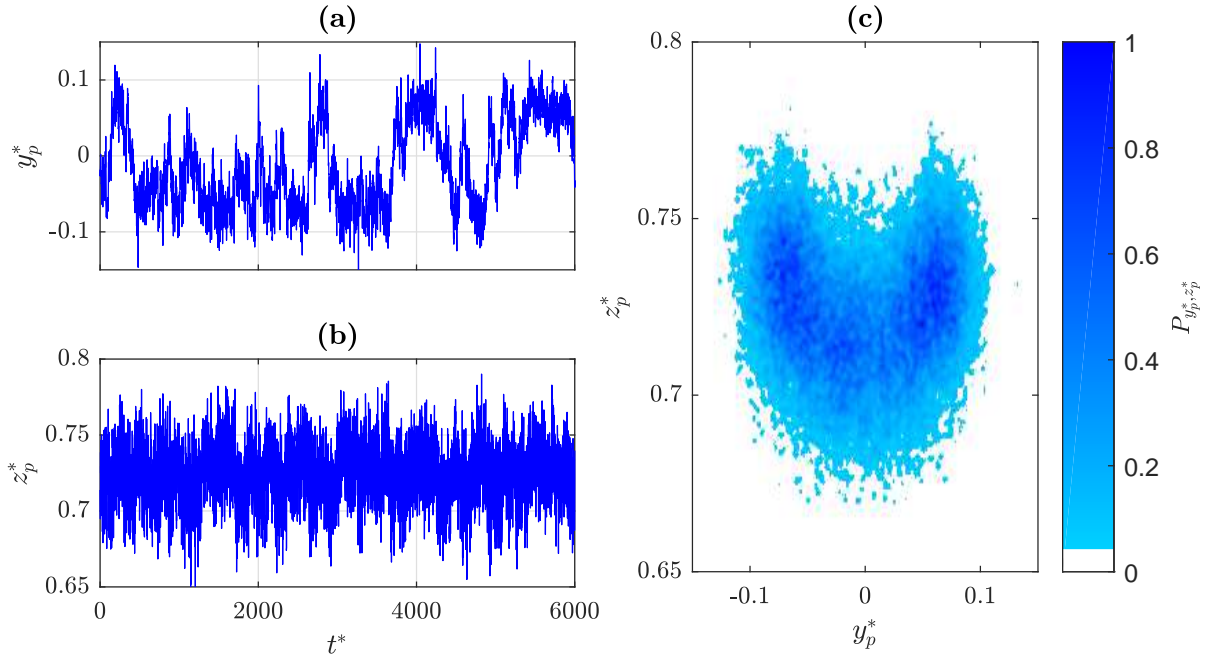
Figure 3: Time series of (a) y_p^* and (b) z_p^*. (c) Normalized 2D PDF of (y_p^*, z_p^*) for the reference flow.

anti-correlated. From the time-series of the pressure center G_p in Fig. 3(a-b), the 2D probability density function (PDF) is computed (c). As expected at such a Reynolds number two regions are more often explored by the pressure center: One located in the negative part of the y^*-axis and the other one in the positive part.

Defining two thresholds based on the pressure center and using conditional-averaging, it is then possible to describe three main modes for the wake, as shown in Fig. 4. The thresholds, denoted $y_{p,N}^*$ and $y_{p,P}^*$, are computed as:

$$y_{p,N}^* = 0.5 y_{p\,\mathrm{max}(P_{y_p^*|y_p^*<\overline{y_p^*}})}^* \text{ and } y_{p,P}^* = 0.5 y_{p\,\mathrm{max}(P_{y_p^*|y_p^*>\overline{y_p^*}})}^*, \tag{3}$$

where P_X is the PDF of the variable X. The 0.5 factor is arbitrarily chosen. Comparing y_p^* to these thresholds we can distinguish between negative (N), positive (P) and transient (T) states, where respectively $y_p^* < y_{p,N}^*$, $y_p^* > y_{p,P}^*$ and $y_{p,N}^* < y_p^* < y_{p,P}^*$. The two first states correspond to the RSB modes while the latter is a much more unstable symmetric state. This is the reason why we consider that the wake exhibits a multi-modal dynamics afterwards. The modes are defined regarding the pressure center but they can also be identified through the recirculation barycenter tracking.

4 Control of the wake dynamics

4.1 Closed-loop control law

The actuation frequency f_{act}^* and the mean jet velocity $\overline{u_{jet}}$ are set before turning the control on. For each jets group we define a range for the spanwise location of the recirculation intensity barycenter y_{rec}^* for which the group is active as shown by Fig. 5. Out of its defined range a group does not blow. The instantaneous velocity fields and y_{rec}^* are computed in real-time. The control variable is updated every
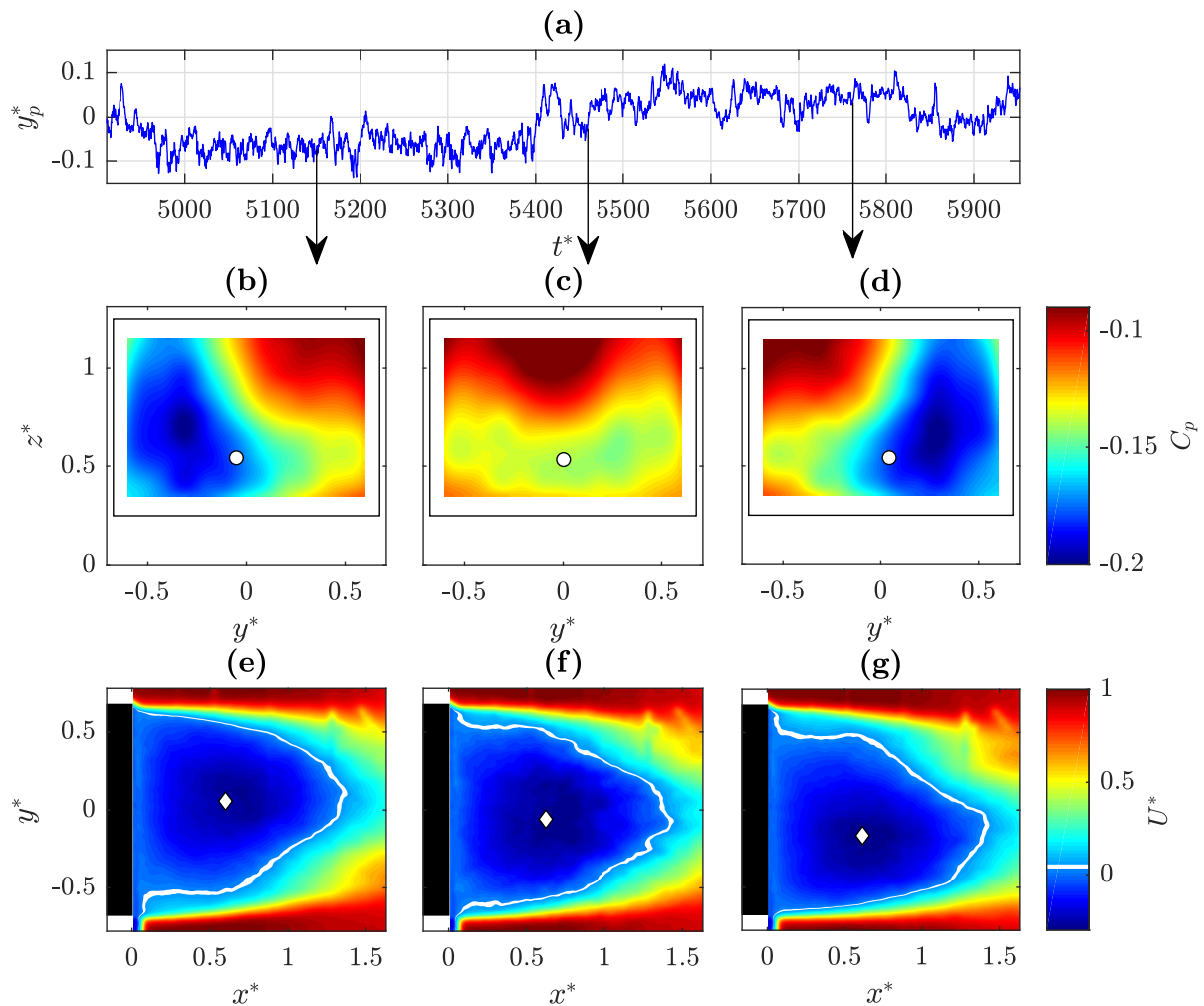
Figure 4: (a) Time series of y_p^* showing the switching of the wake from a RSB mode to another one. Conditional averages of the pressure coefficient at the rear body and the streamwise component of the velocity field at $z^* = 1$ for the modes (b-e) N, (c-f) T and (d-g) P. The average position of the pressure center G_p (white circle) and of the recirculation barycenter G_{rec} (white diamond) are also displayed.

ΔT seconds. To summarize, the principle of the actuation consists in blowing in the region where the recirculation barycenter is detected.

Two types of actuation are used in the closed-loop experiments: A continuous blowing or a pulsed blowing with different actuation frequencies f_{act}^*. In the following, we will focus on two actuation frequencies: $f_{act}^* = 0.2$ and $f_{act}^* = 0.8$.

4.2 Stabilization of the wake

One can see in Fig. 6 that all closed-loop experiments lead to a clear reduction of the recirculation area, i.e. of the size of the wake. We can also notice the strong influence of the type of actuation as pulsed actuations, and especially with an actuation pulsation frequency of $f_{act}^* = 0.2 \, (-36\%)$, are more efficient than continuous blowing (-14%).

The objective of these experiments was also to control the wake dynamics which can be characterized by the fluctuations of the spanwise location of the recirculation barycenter. The natural fluctuations of the pressure and recirculation barycenters are shown respectively on Fig. 7(a-c). One can see the switching
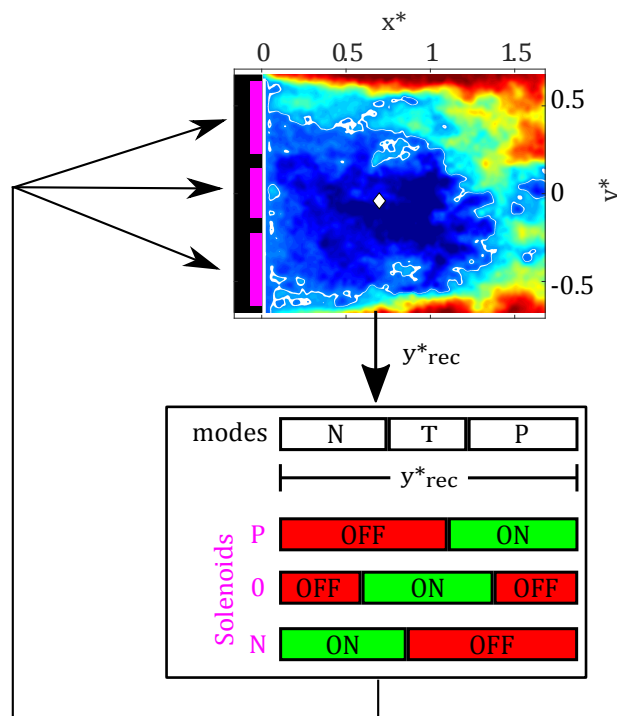
Figure 5: Schema of the closed-loop control law based on the recirculation barycenter tracking (white diamond) computed from the velocity fields.

of the wake over relatively large time scales together with small-scales high-frequencies oscillations. The signal for $y_{rec}^*(t)$ appears smoother because of the much lower sampling frequency. When the closed-loop actuation is triggered, the dynamics of the barycenters [Fig. 7(b-d)] is completely changed. Instead of random large and small fluctuations, the oscillations of the barycenters become very regular and periodic. It is now imposed by the characteristic time-scale of the closed-loop.

4.3 Creation of a multistable state

Another way to characterize the dynamics of the wake is to look at the full trajectory of the pressure barycenter over the rear part of the model. The trajectories appears chaotic and indeed it was shown recently [11] that the pressure barycenter follows a chaotic motion between two strange attractors that are clearly visible in a 2D probability density function (PDF), as shown in Fig. 3(c).

When the recirculation barycenter is tracked and blown with a continuous blowing by the closed-loop algorithm, the PDF is also completely changed and exhibits two strong foci, as shown in Fig. 8(a). This modification is also observed with a "high" frequency actuation ($f_{act}^* = 0.8$) in Fig. 8(b). Interestingly, the PDF is also strongly modified by a lower actuation frequency ($f_{act}^* = 0.2$) [Fig. 8(c)]. In this case, one can see a butterfly shape with four attractors instead of two for all other cases. These results suggest the occurrence of multi-modal state with a right-left oscillation *and* a top-bottom oscillation. This is also the configuration with the smallest time-averaged recirculation area.

5 Conclusions

To our knowledges, it is the first implementation of a closed-loop flow control in a wind tunnel facility based on the velocity fields. Using real-time PIV, it was possible to settle a closed-loop opposition algorithm based on the instantaneous computation of the spanwise position of the recirculation barycenter.
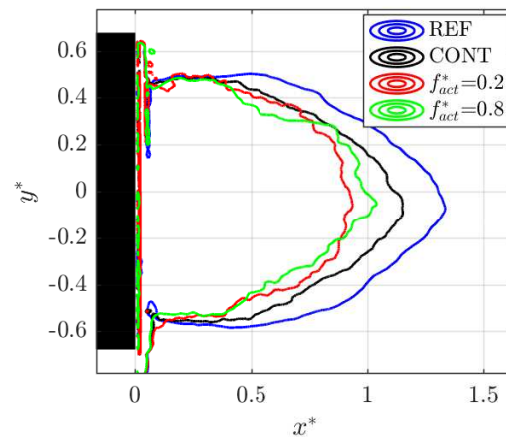
Figure 6: Contours of the recirculation area for the reference (blue), the continuous blow (black), $f_{act}^* = 0.2$ (red) and $f_{act}^* = 0.8$ (green).

The spanwise oscillation of the location of the recirculation (and pressure) barycenter was then forced into a regular periodic oscillation forced by the time-scale of the algorithm. Moreover, a much larger reduction of the recirculation area is found when a pulsed actuation is used in the closed-loop control experiments. As expected, the 2D PDF of trajectories exhibits well-defined stable foci points for most of the configurations, except for the $f_{act}^* = 0.2$ which shows a four attractors configuration suggesting a multi-modal configuration with a right-left oscillation together with a top-bottom oscillation of the wake.

6   Acknowledgements

References

[1] S. R. Ahmed, G. Ramm, and G. Faltin. Some Salient Features Of The Time-Averaged Ground Vehicle Wake. In *SAE Technical Paper*. SAE International, 1984.

[2] J.-F. Beaudoin, O. Cadot, J.-L. Aider, K. Gosse, P. Paranthoën, B. Hamelin, M. Tissier, D. Allano, I. Mutabazi, M. Gonzales, et al. Cavitation as a complementary tool for automotive aerodynamics. *Exp. Fluids*, 37(5):763–768, 2004.

[3] F. Champagnat, A. Plyer, G. Le Besnerais, B. Leclaire, S. Davoust, and Y. Le Saint. Fast and accurate PIV computation using highly parallel iterative correlation maximization. *Exp. Fluids*, 50:1169–1182, 2011.

[4] Y. Eulalie. *Aerodynamic analysis and drag reduction around an Ahmed bluff body*. PhD thesis, Université de Bordeaux, Bordeaux, France, Dec 2014.

[5] N. Gautier and J.-L. Aider. Feed-forward control of a perturbed backward-facing step flow. *J. Fluid Mech.*, 759:181–196, 2014.
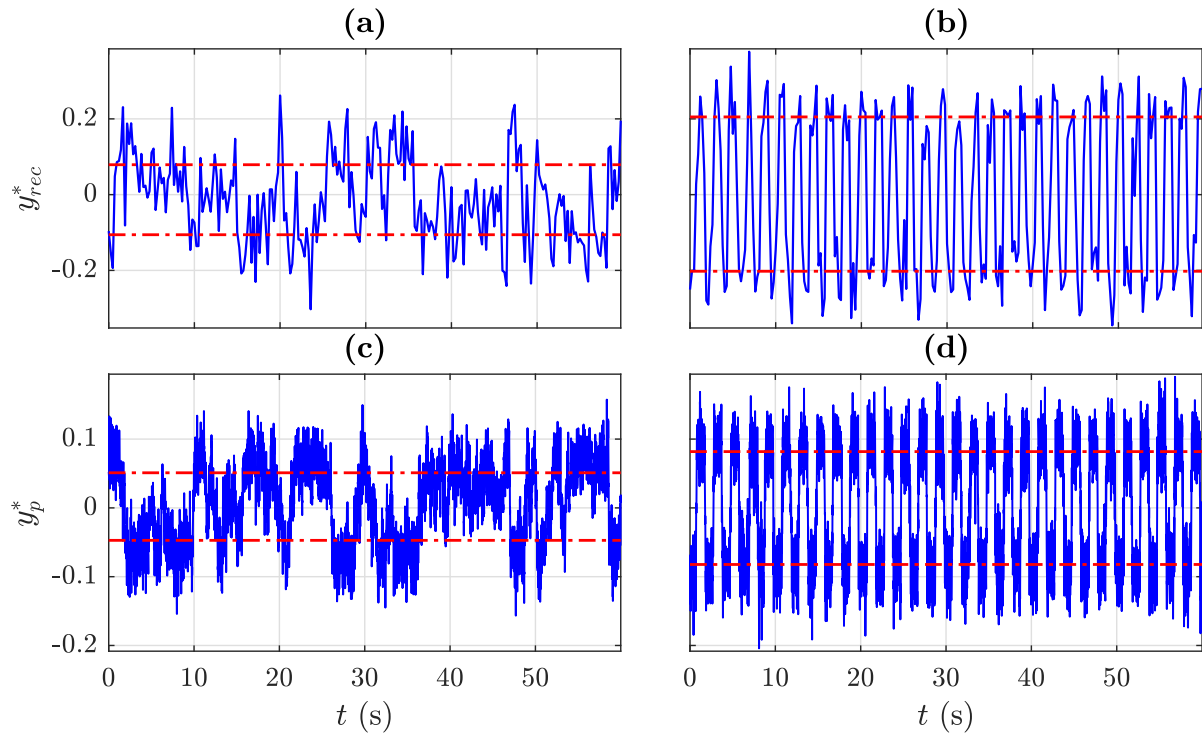
Figure 7: Spanwise location of the recirculation barycenter and the pressure center for (a-c) the reference flow compared to (b-d) the controlled flow with pulsed jets at $f_{act}^* = 0.8$, together with the PDF peaks location (red dash-dotted lines).

[6] N. Gautier and J.-L. Aider. Frequency-lock reactive control of a separated flow enabled by visual sensors. *Exp. Fluids*, 56(1):1–10, 2015.

[7] N. Gautier and J.-L. Aider. Real-time planar flow velocity measurements using an optical flow algorithm implemented on GPU. *J. Vis.*, 18:277–286, 2015.

[8] M. Grandemange, M. Gohlke, and O. Cadot. Turbulent wake past a three-dimensional blunt body. Part 1. Global modes and bi-stability. *J. Fluid Mech.*, 722:51–84, 2013.

[9] C. Pan, D. Xue, Y. Xu, J. Wang, and R. Wei. Evaluating the accuracy performance of Lucas-Kanade algorithm in the circumstance of PIV application. *Sci. China Phys. Mech.*, 58:104704, 2015.

[10] A. Plyer, G. Le Besnerais, and F. Champagnat. Massively parallel Lucas Kanade optical flow for real-time video processing applications. *J. Real-Time Image Proc.*, 11(4):713–730, 2016.

[11] E. Varon, Y. Eulalie, S. Edwige, P. Gilotte, and J.-L. Aider. Chaotic dynamics of large-scale structures in a turbulent wake. *Phys. Rev. Fluids*, 2:034604, 2017.
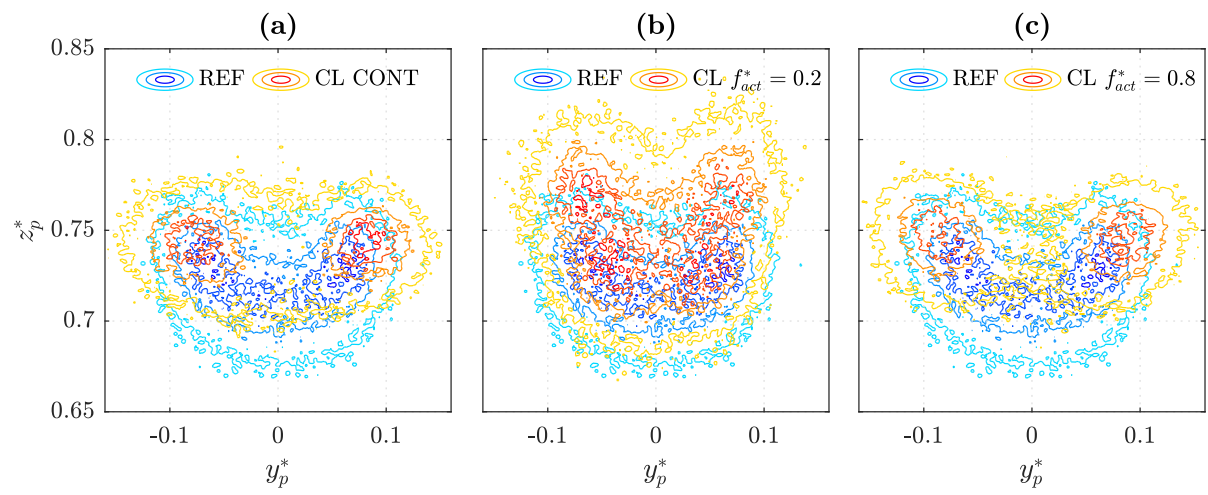
Figure 8: 2D PDF contour of (y_p^*, z_p) for the reference flow and various forcing: (a) continuous blowing, (b) pulsed blowing for $f_{act}^* = 0.2$ and (c) $f_{act}^* = 0.8$.